Characterization of Spin-Orbit Torque Efficiency in Magnetic Heterostructures with Perpendicular Magnetic Anisotropy via Spin-Torque Ferromagnetic Resonance

Jinwu Wei,[1,2,3] Congli He,[4] Xiao Wang,[1,2] Hongjun Xu,[1,2,3] Yizhou Liu,[1,2] Yao Guang,[1,2] Caihua Wan,[1,2] Jiafeng Feng,[1,2] Guoqiang Yu,[1,2,3,*] and Xiufeng Han[1,2,3]

[1] *Beijing National Laboratory for Condensed Matter Physics, Institute of Physics, Chinese Academy of Sciences, Beijing 100190, China*

[2] *Center of Materials Science and Optoelectronics Engineering, University of Chinese Academy of Sciences, Beijing 100049, China*

[3] *Songshan Lake Materials Laboratory, Dongguan, Guangdong 523808, China*

[4] *Institute of Advanced Materials, Beijing Normal University, Beijing 100875, China*

(Received 11 September 2019; revised manuscript received 5 January 2020; accepted 28 February 2020; published 17 March 2020)

Characterization of spin-orbit torques (SOTs) in the perpendicular magnetic anisotropy (PMA) system is of great importance for fundamental studies and technological applications in spintronic devices. Here, we report a spin Hall magnetoresistance (SMR) based spin-torque ferromagnetic resonance (ST FMR) study of SOT efficiency in perpendicularly magnetized W/$Co_{40}Fe_{40}B_{20}$/MgO structures. A full analysis of the ST FMR spectrum is developed for the PMA sample. A typical ST FMR spectrum of the PMA system shows two resonance modes, i.e., in-plane and out-of-plane magnetization precession modes. By performing modulation of the damping measurement for the in-plane mode, the dampinglike torque efficiency is determined to be -0.38, which is consistent with the reference value obtained in samples with in-plane magnetic anisotropy. The dampinglike torque efficiency of -0.31 is also obtained from the out-of-plane resonance mode, in which the significant contribution of the spin-pumping-induced inverse spin Hall effect is carefully considered. The obtained values of dampinglike torque efficiency by different means are consistent with each other. The present work provides useful insights to determine the dampinglike torque efficiency of the PMA sample via ST FMR measurements.

DOI: 10.1103/PhysRevApplied.13.034041

I. INTRODUCTION

Spin-orbit torque (SOT) is a promising candidate mechanism to drive magnetization switching [1–3], magnetization oscillation [4–6], domain wall and skyrmion motion [7–9]. In a heavy metal-ferromagnetic metal (HM-FM) bilayer, the current-induced SOT originates from the spin current due to the spin Hall effect (SHE) and/or Rashba effect. The SOT usually has two orthogonal components [10–12], i.e., dampinglike (DL) and fieldlike (FL) torque, which take the form of $\gamma h_{\mathrm{DL}} \mathbf{m} \times \boldsymbol{\sigma} \times \mathbf{m}$ and $\gamma h_{\mathrm{FL}} \mathbf{m} \times \boldsymbol{\sigma}$, respectively. Here, γ is the gyromagnetic ratio; h_{DL} and h_{FL} are the effective fields of DL torque and FL torque, respectively; $\mathbf{m}$ is the unit vector of magnetization; and $\boldsymbol{\sigma}$ is the polarization direction of spin current. The dampinglike torque can be used to switch both in-plane and out-of-plane magnetization [13,14]. From the application point of view, a study of the SOT-driven perpendicular magnetization switching is of importance due to the potential applications of perpendicular magnetic anisotropy (PMA) materials in high-density and ultrafast devices [15,16]. To better employ the SOT in perpendicular magnetization manipulation, it is vital to quantitatively characterize the SOT efficiency.

Several techniques have been developed to characterize the SOT in a typical HM-FM bilayer, including harmonic Hall voltage analysis [17,18], spin-torque ferromagnetic resonance (ST FMR) [19–21], and the magneto-optical Kerr effect [22,23]. Among these techniques, ST FMR is an effective and convenient method, which is therefore extensively applied to SOT characterization. When a radiofrequency (rf) current, I_{rf}, is applied to a HM-FM bilayer device, the magnetization is oscillated by the current-induced SOT, resulting in an oscillation of resistance (R_{rf}) due to the magnetoresistance effect. A dc rectification voltage is thus generated from the mixing of the I_{rf} and R_{rf}. To obtain a strong rectification voltage, and thus, a strong ST FMR spectrum, the magnetoresistance

*guoqiangyu@iphy.ac.cn

effect must be large enough to produce a necessary resistance change. In general, the anisotropy magnetoresistance (AMR) in the HM-FM with a relatively thick FM layer can lead to a sizable signal. The AMR significantly decreases with the FM thickness, resulting in a reduction of the ST FMR signal with FM thickness. For this reason, previous ST FMR measurements of SOT efficiency are mainly concentrated on the HM-FM bilayers with thick FMs. The thickness requirement limits the ST FMR measurements to HM-FM bilayers with in-plane magnetic anisotropy (IMA) [24,25] or bulk PMA materials [26]. For a general HM-FM bilayer with an interfacial PMA, in which the FM layer is typically very thin, the small AMR value challenges the ST FMR measurement.

Recently, a new magnetoresistance effect, named spin Hall magnetoresistance (SMR), was observed in HM-ferromagnetic insulator (FI) and HM-FM bilayers [27,28]. The SMR originates from the spin Hall effect and is determined by the angle between magnetization and the polarization direction of spin current. Thanks to the SMR, a strong ST FMR spectrum can still be observed in the HM-FI and perpendicular HM-FM bilayer with an ultrathin FM layer, although the AMR is absent [28–30]. This SMR-based ST FMR allows the study of the high-frequency resonance properties of FI and ultrathin nanosized magnetic films. Moreover, it is also used to explore the SOT efficiency in the HM-FI bilayer with an IMA [28,31]. However, it is rarely applied to study the SOT in the HM-FM bilayer with a PMA, which is vital for SOT applications.

Here, we study the SOT efficiency in perpendicularly magnetized W/$Co_{40}Fe_{40}B_{20}$/MgO structures by a ST FMR technique. In Sec. II, we develop a full analysis of SMR-based ST FMR, which applies to both IMA and PMA systems. Through the analysis of the angular dependence of the ST FMR signal, we dissect the contributions from various origins to the measured voltage and extract the SOT efficiencies. In Sec. III, we briefly introduce the experiments. In Sec. IV, we get the SOT efficiency in IMA samples as a reference and then we study the full ST FMR spectra in the PMA system. We observe in-plane and out-of-plane magnetization precession modes, and systematically analyze the SOT efficiencies through different methods. These results are consistent with each other and can help to understand the properties of PMA samples to facilitate their practical applications.

II. THEORY OF SMR-BASED ST FMR

In this section, we develop a full analysis of the ST FMR spectrum suitable for both IMA and PMA samples. The ST FMR signal can be written as $V(t) = I_0 \cos(\omega t) R(\omega t)$, where I_0 is the amplitude of $I_{\rm rf}$ with a frequency of $\omega/2\pi$. The resistance can be obtained based on the SMR expression [32,33], $R_{\rm SMR} = R_z + \Delta R \cos^2\theta \sin^2\varphi$. Here,

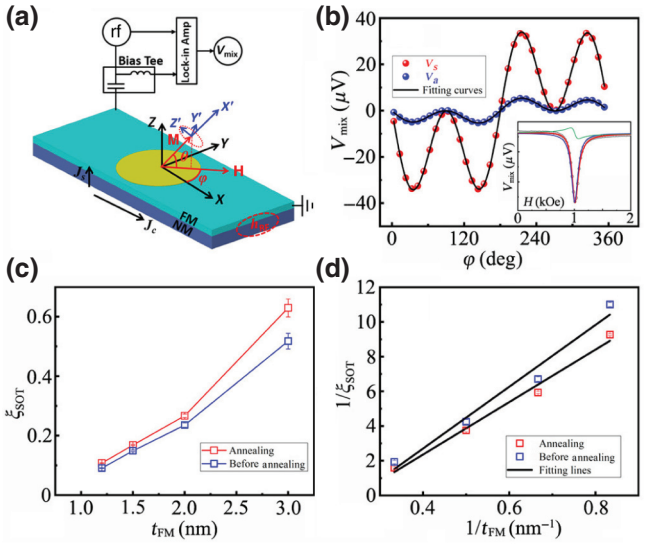

FIG. 1. (a) Schematic of ST FMR measurement setup, including a bias tee, a microwave signal generator, and a lock-in amplifier. J_c denotes the charge current of the sample, and J_s denotes the spin current along the normal direction of films. External field H is applied in plane at angle φ with respect to the X axis. (b) Angular dependence of V_s and V_a for the annealed sample with IMA and thickness $t_{\rm FM} = 1.2$ nm. Inset: typical ST FMR spectrum of the same sample measured at $\varphi \approx 35°$; excited frequency is 4 GHz. Open circles indicate measured data, which are fitted by symmetric (blue solid curve) and antisymmetric (green solid curve) components. (c) SOT efficiency as a function of FM thickness $t_{\rm FM}$. (d) Reciprocal of SOT efficiency, $\xi_{\rm SOT}^{-1}$, as a function of the reciprocal FM thickness, $t_{\rm FM}^{-1}$, for all samples, except for PMA samples.

$\Delta R = R_y - R_x$ and R_i is the resistance measured when the magnetization is saturated parallel to $i = x, y, z$, which is characterized by $R_y < R_z \approx R_x$. θ and φ are the polar and azimuthal angles of magnetization **M**, respectively, as shown in Fig. 1(a). The resistance oscillation of the device can be reflected by the oscillating angle $\varphi(t) = \varphi + \varphi_c \cos(\omega t + \varphi_0)$ and $\theta(t) = \theta + \theta_c \cos(\omega t + \theta_0)$. φ_c and θ_c are the cone angles of magnetization precession, which are usually much smaller than those of φ and θ under the condition of small-amplitude magnetization precession. φ_0 and θ_0 are the phase lag between magnetization precession and the driving force, which are neglected because the current-induced spin torques directly drive magnetization. The $\sin\varphi$ and $\cos\theta$ terms can be expanded by using the Taylor series, and then the mixing voltage can be reduced to

$$V_{\rm mixing} = -\frac{I_0 \Delta R}{2}(\cos^2\theta \sin 2\varphi\, \varphi_c - \sin^2\varphi \sin 2\theta\, \theta_c). \quad (1)$$

Here, two time-dependence terms with frequencies of ω and 2ω are ignored. The $V_{\rm mixing}$ value is dependent on

the amplitude of I_{rf}, the SMR of the sample, the rotation angle φ and polar angle θ of **M**, and the cone angles of magnetization precession φ_c and θ_c.

To simplify the analysis, two Cartesian coordinates are used. As shown in Fig. 1(a), the X, Y, Z coordinate is fixed with respect to the device. The X', Y', Z' coordinate is a moving coordinate with the X' axis along the **M** and Y' axes in the X-Y plane. We only consider that external field **H** rotates in the film plane under angle φ with respect to the X axis. θ is the polar angle of **M** deviated from the X-Y plane. The cone angles φ_c and θ_c of magnetization precession can be estimated by $\varphi_c \approx \sin\varphi_c = M_{y'}/M_0$ and $\theta_c \approx \sin\theta_c = M_{z'}/M_0$; here, $M_{y'}$ and $M_{z'}$ denote the projection components of the saturation magnetization M_0 onto Y' and Z' axes, respectively. The derivations of φ_c and θ_c are given in Appendix A. By substituting the cone angles into Eq. (1), the SMR-based ST FMR signal can be written as

$$V_{\text{mixing}} = V_{\text{offset}} + V_s\frac{\Delta H^2}{(H-H_r)^2+\Delta H^2} + V_a\frac{\Delta H(H-H_r)}{(H-H_r)^2+\Delta H^2}, \tag{2}$$

where V_{offset} is the offset value of the measured voltage and V_s and V_a are the coefficients of symmetric and antisymmetric components, respectively, which are determined by $V_{s(a)} = A_{s(a)}\cos\varphi\sin2\varphi + B_{s(a)}\sin\varphi\sin2\varphi + C_{s(a)}\sin\varphi$. Here, $A_s = \lambda_0 h_{\text{DL}}(\cos^2\theta - \sin^2\theta\cos\theta)$, $B_s = \lambda_0(h_{\text{FL}} + h_{Oe})\sin\theta\cos\theta(1-\cos\theta)$, $C_s = \lambda_0 h_{\text{DL}}\sin\theta\sin2\theta$, $A_a = \lambda_0(h_{\text{FL}} + h_{\text{Oe}})(\lambda_1\cos^2\theta - \sin^2\theta\cos\theta/\lambda_1)$, $B_a = \lambda_0 h_{\text{DL}}\sin\theta\cos\theta(\lambda_1\cos\theta - 1/\lambda_1)$, $C_a = \lambda_0(h_{\text{FL}} + h_{\text{Oe}})\sin\theta\sin2\theta/\lambda_1$, $\lambda_0 = -I_0\Delta R/(2\alpha)/(H_{y'} + H_{z'})$, and $\lambda_1 = (H_{z'}/H_{y'})^{1/2}$. Here, α is the Gilbert damping constant and $H_{y'}$ and $H_{z'}$ are the static effective fields induced by the external field and magnetic anisotropy field in the X',Y',Z' coordinate, respectively.

In the following, we discuss two common precession modes, according to the orientation of magnetization. One is the in-plane (IP) precession mode, in which the magnetization is oriented in the film plane by an external in-plane magnetic field for the PMA and IMA samples. The other one is the out-of-plane (OOP) precession mode for the PMA samples. In this case, the FMR happens when the magnetization deviates from the PMA axis at a small in-plane magnetic field. For the IP precession mode, the polar angle is $\theta = 0$ and the effective fields are $H_{y'} = H_r$ and $H_{z'} = H_r + M_0$. Therefore, the coefficients of the symmetric term and antisymmetric terms can be reduced to

$$V_s = \lambda_0\frac{\hbar}{2e}\frac{\xi_{\text{DL}}J_c}{\mu_0 M_0 t_{\text{FM}}}\cos\varphi\sin2\varphi, \tag{3a}$$

$$V_a = \lambda_0\sqrt{1+\frac{M_0}{H_r}}\left(\frac{J_c t_{\text{HM}}}{2} + \frac{\hbar}{2e}\frac{\xi_{\text{FL}}J_c}{\mu_0 M_0 t_{\text{FM}}}\right)\cos\varphi\sin2\varphi. \tag{3b}$$

Here, $\xi_{\text{DL(FL)}}$ denotes the dampinglike (fieldlike) torque efficiency. Eq. (3) indicates that the symmetric and antisymmetric components of mixing voltage obey the same angular dependence of $\cos\varphi\sin2\varphi$. Therefore, the SOT efficiency can be assessed by the V_s/V_a ratio [10],

$$\xi_{\text{SOT}} = \frac{V_s}{V_a}\frac{e}{\hbar}\mu_0 M_0 t_{\text{FM}} t_{\text{HM}}\sqrt{1+\frac{M_0}{H_r}}. \tag{4}$$

When the FL torque is much smaller than the torque of the Oersted field, one will have $\xi_{\text{SOT}} = \xi_{\text{DL}}$. While the FL torque is comparable to the torque of the Oersted field, ξ_{SOT} will depend on t_{FM}, and it can be expressed as [10]

$$\frac{1}{\xi_{\text{SOT}}} = \frac{1}{\xi_{\text{DL}}}\left(1+\frac{\hbar}{e}\frac{\xi_{\text{FL}}}{\mu_0 M_0 t_{\text{FM}} t_{\text{HM}}}\right). \tag{5}$$

The efficiency of DL torque and FL torque can be determined by the ferromagnet thickness dependence of ξ_{SOT}. The DL torque mainly originates from the SHE in the bulk region of HM, so the DL torque efficiency is proportional to the spin Hall angle, i.e., $\xi_{\text{DL}} = T_{\text{in}}\theta_{\text{SH}}$; here, T_{in} denotes the interfacial spin transparency [10].

For the OOP precession mode, the magnetization precession axis tilts out of the film plane. Eq. (2) is thus correlated with polar angle θ. Notably ΔR_{SMR} is reduced when the magnetization is oblique to the plane due to the PMA (see Appendix B for details), which leads to the ST FMR voltage for the OOP mode being weaker than that for the IP mode. For the PMA systems, the effective fields are expressed as $H_{y'} = H\cos\theta - H_1\sin^2\theta - H_2\sin^4\theta$ and $H_{z'} = H\cos\theta + H_1\cos2\theta + H_2(3\sin^2\theta\cos^2\theta - \sin^4\theta)$. Here, H_1 and H_2 are the first- and second-order PMA fields, and H is the external magnetic field applied in the film plane [29,34]. The symmetric and antisymmetric components of mixing voltage have the following angular dependence:

$$V_{s(a)} = A_{s(a)}\cos\varphi\sin2\varphi + B_{s(a)}\sin\varphi\sin2\varphi + C_{s(a)}\sin\varphi, \tag{6}$$

where $A_{s(a)}$, $B_{s(a)}$, and $C_{s(a)}$ are coefficients described previously. Different from the IP mode, the angular dependences of $\sin\varphi\sin2\varphi$ and $\sin\varphi$ appear in the OOP mode.

In addition to the mixing voltage, a dc voltage from the inverse spin Hall effect (ISHE) due to spin pumping can also contribute to the measured signal. Spin pumping provides a route to generate a spin current through magnetization precession. In the HM-FM system, a spin current is pumped into the HM layer from the FM under the FMR condition and is then converted

into an electric voltage through the ISHE. Generally, the ISHE voltage can be described by a Lorentzian equation, $V(H) = V_{\mathrm{ISHE}}\{\Delta H^2/[(H-H_r)^2+\Delta H^2]\}$, and the angle φ dependence of V_{ISHE} has two terms, i.e., $V_{\mathrm{ISHE}} \sim F_y \cos\varphi \sin 2\varphi + F_z \sin\varphi$ [35]. The former is due to y-directional excitation (rf Oersted field and fieldlike torque), which results in the same signal as that of the ST FMR signal. This term can be neglected in this work (see Appendix C for details). The latter arises from z-directional excitation (rf dampinglike torque), which is reported in many studies and can be expressed as [35,36]

$$V_{\mathrm{ISHE}} = -\frac{e\lambda_{\mathrm{sd}} l_{\mathrm{HM}} \theta_{\mathrm{SH}} g_{\uparrow\downarrow} \omega}{2\pi \sigma_{\mathrm{HM}} t_{\mathrm{HM}}} \tanh\left(\frac{t_{\mathrm{HM}}}{2\lambda_{\mathrm{sd}}}\right) \sin^2\theta_c \sin\varphi, \tag{7}$$

where λ_{sd}, l_{HM}, σ_{HM}, and θ_{SH} are the spin diffusion length, length dimension, conductivity, and spin Hall angle of the heavy metal; θ_c is the cone angle of magnetization precession.

III. EXPERIMENTS

Samples consisting of W(5 nm)/$Co_{40}Fe_{40}B_{20}$(t nm)/MgO(2 nm)/Ta(2 nm), with $t = 1.0$, 1.2, 1.5, 2.0, and 3.0, are deposited on silicon substrate by means of magnetron sputtering. All samples are annealed under vacuum at 250 °C for 0.5 h to enhance the PMA. The annealed sample with a thickness of 1.0 nm shows a strong PMA. The magnetic properties of all samples and device fabrication have been described in previous work [29]. All samples have a sizable SMR, and the AMR is negligible. Figure 1(a) shows the setup for ST FMR measurements. The microwave source provides a stimulated I_{rf} with a frequency ranging from 100 kHz to 20 GHz, which is modulated by a low-frequency sinusoidal wave. A bias tee is used to separate the dc signal from the mixed signal.

IV. RESULTS AND DISCUSSION

A. SOT efficiency in the IMA system

Before studying the PMA samples, we present the experimental results and SOT efficiency analysis for the sample with an IMA to provide a reference for comparison. The typical ST FMR spectrum of the sample with the IMA is shown in the inset of Fig. 1(b). The measured V_{mix} data are fitted by Eq. (2), which have symmetric and antisymmetric parts. According to Eq. (3), the symmetric part, V_s, is correlated to the DL torque, while the antisymmetric part, V_a, is correlated to the FL torque and Oersted field. The angle dependences of coefficients V_s and V_a for the same sample with $t_{\mathrm{FM}} = 1.2$ nm are shown in Fig. 1(b), which exhibit a smooth angular dependence of $\cos\varphi\sin2\varphi$. The SOT efficiency can be estimated from the ratio V_s/V_a and calculated by using Eq. (4). As the thickness t_{FM} increases, the SOT efficiencies for the as-grown and annealed samples increase [see Fig. 1(c)], which indicates that the W/$Co_{40}Fe_{40}B_{20}$/MgO/Ta samples have a significant contribution from FL torque. In terms of the t_{FM} thickness dependence of SOT efficiency, a linear fit between $\xi_{\mathrm{SOT}}{}^{-1}$ and $t_{\mathrm{FM}}{}^{-1}$ is performed, as shown in Fig. 1(d). We fit the results using Eq. (5) and obtain $\xi_{\mathrm{DL}} = -0.35 \pm 0.016$ and $\xi_{\mathrm{FL}} = -0.05 \pm 0.001$ for the as-grown samples and $\xi_{\mathrm{DL}} = -0.36 \pm 0.002$ and $\xi_{\mathrm{FL}} = -0.05 \pm 0.001$ for the annealed samples. The ξ_{DL} value changes slightly after annealing, which is related to the change of interfacial spin transparency. These obtained values are consistent with previous works ($|\xi_{\mathrm{DL}}| = 0.33 \sim 0.4$ in the W/$Co_{40}Fe_{40}B_{20}$MgO structure) [24,25,37]. Moreover, the samples present a remarkable FL torque, which is also consistent with previous results [38].

B. SOT efficiency in the PMA system

We now present the results for the PMA samples. Figures 2(a) and 2(b) show the ST FMR spectra for the annealed sample with $t_{\mathrm{FM}} = 1.0$ nm. The ST FMR spectra show two resonance peaks; this pattern is different from that for the sample with IMA. Similar to previous work [29], the two resonance peaks correspond to the in-plane and out-of-plane magnetization precession modes, respectively. We fit the spectra using two sets of Eq. (2). Figure 2(c) shows the measured voltage mapping as a function of the external field and rotational angle φ. For the IP mode, the main negative peaks appear at $\varphi = 35°$ and 145°, and two positive peaks at 215° and 325°, following the angle dependence of $\cos\varphi\sin2\varphi$. However, for the OOP mode, the main peaks occur at $\varphi = 90°$ and 270°, respectively, which obey the angle dependence of $\sin\varphi$. According to Eqs. (6) and (7), both V_{mixing} and V_{ISHE} have a $\sin\varphi$-dependent part. Previous reports [21,39] show that the spin-pumping-induced V_{ISHE} typically plays a minor role in the sample with an IMA. However, this contribution is enhanced when an external magnetic field is applied oblique to the film and enables the out-of-plane magnetization [40]. Therefore, the spin-pumping contribution should be carefully considered. In the following, we demonstrate that DL torque efficiency can be separately determined through analyzing the resonance peaks for IP and OOP modes.

1. In-plane mode

Figures 3(a) and 3(b) show the angular dependence of the symmetric and antisymmetric components of the IP mode, respectively, which are fitted through Eq. (6). Apparently, the $\cos\varphi\sin2\varphi$ term dominates the angular dependence. The coefficients $A_{s(a)}$ can be simplified, as the angle is $\theta = 0$, and the ratio A_s/A_a gives rise to a SOT efficiency that is analogous to Eq. (4). The SOT efficiency can

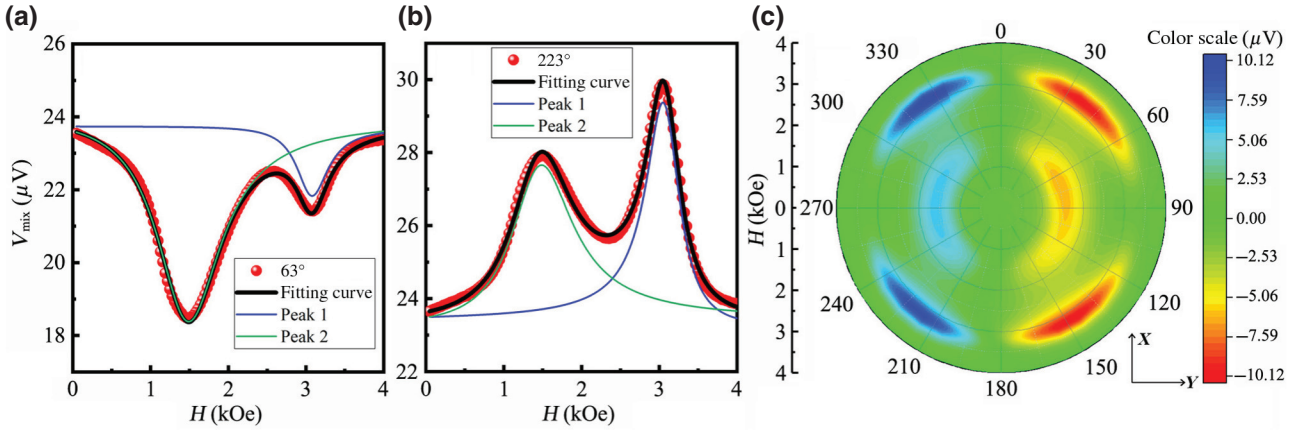

FIG. 2. Experimental ST FMR spectra for the annealed sample with $t_{FM} = 1.0$ nm measured at angles $\varphi = 63°$ (a) and 223° (b). This sample has a strong PMA. Black solid curves represent the fitting of measured data through the superposition of two sets of Eq. (2). Peak 1 (blue curve) and peak 2 (green curve) represent the in-plane resonance mode and out-of-plane resonance mode, respectively. (c) Color map of ST FMR signal as a function of rotational angle φ and external field H. Red (blue) color represents negative (positive) voltage.

be expressed as

$$\xi_{SOT} = \frac{A_s}{A_a}\frac{e}{\hbar}\mu_0 M_0 t_{FM} t_{HM}\sqrt{1+\frac{H_1}{H_r}}. \tag{8}$$

Here, H_1 is the first-order PMA field. According to Eq. (8), we get $\xi_{SOT} = -0.043$ for the sample with PMA. When we consider $\xi_{DL} = -0.36$ (the reference value), the FL torque efficiency can be extracted as $\xi_{FL} = -0.07$ by using Eq. (8). This value is reasonably consistent with the reference value ($\xi_{FL} = -0.05$), indicating the validity of the analysis for the in-plane mode.

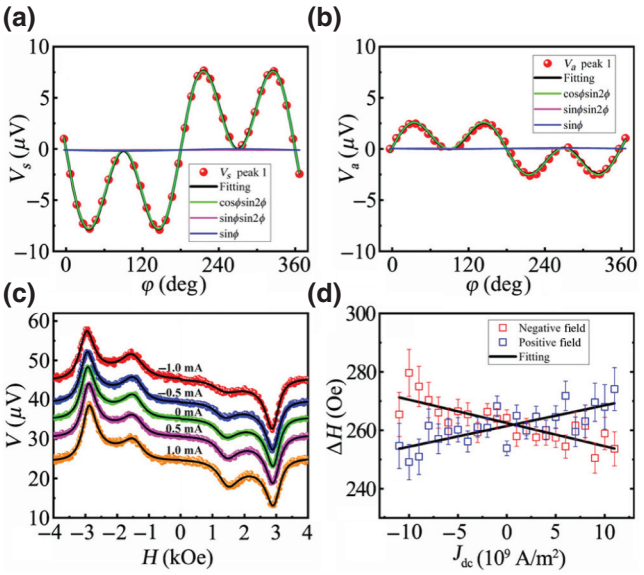

FIG. 3. Angular dependence of symmetric (a) and antisymmetric (b) components of IP mode, which are mainly dependent on angle relation of cosφsin2φ. (b) ST FMR signal spectra modulated by positive and negative currents. (c) De-embedding relationship of resonance width ΔH as a function of applied J_{dc} in the annealed sample with PMA at $\varphi = 30°$ and $f = 4$ GHz. Black solid lines are linear fits.

To directly determine the DL torque efficiency specific for the PMA sample, we perform a modulation of damping (MOD) measurement [21,40], in which the resonance line width ΔH can be tuned by a dc current in the HM layer. The change of resonance line width can be expressed as

$$\Delta H = \frac{2\pi f}{\gamma}\left[\alpha + \frac{J_{dc}\xi_{DL}\sin\varphi}{(H + 2\pi M_{eff})\mu_0 M_0 t_{FM}}\frac{\hbar}{2e}\right]. \tag{9}$$

Figure 3(c) shows the ST FMR spectra measured at different dc currents. Here, the MOD method is performed at angle $\varphi = 30°$ and an excited frequency of $f = 4$ GHz, and then we obtain the J_{dc} dependence of the line width ΔH for the IP mode. It can be clearly seen that ΔH gradually decreases with an increase in current from -1 mA to $+1$ mA in the negative field. On the contrary, ΔH increases with an increase in current in the positive field. Notably the current density J_{dc} dependence of line width ΔH contains odd and even components with respect to J_{dc}; these components are due to the SOT and Joule heating [41], respectively. A linear relation between ΔH and J_{dc} is extracted, as shown in Fig. 3(d). According to Eq. (9), the linear fitting of ΔH allows the extraction of the DL torque efficiency. We obtain $\xi_{DL} = -0.36 \pm 0.067$ under positive field and $\xi_{DL} = -0.41 \pm 0.065$ under negative field. The averaged value is thus -0.38 ± 0.066, which is consistent with the reference value obtained in the sample with IMA. It is noted that the MOD measurement can remove the spin pumping contribution, which also verifies the validity of the value obtained through the angle dependence measurement in Sec. IV A.

2. Out-of-plane mode

Next, we demonstrate the determination of SOT efficiency through analyzing the resonance peak for the OOP mode. Figures 4(a) and 4(b) show the angular dependences of the symmetric and antisymmetric coefficients of OOP mode, respectively, which are fitted by the equation $V_{s(a)} = A_{s(a)}\cos\varphi\sin2\varphi + B_{s(a)}\sin\varphi\sin2\varphi + C_{s(a)}\sin\varphi$. Obviously, V_s and V_a also have a $\sin\varphi$ term in addition to the $\cos\varphi\sin2\varphi$ term. If the contribution of $C_{s(a)}\sin\varphi$ entirely originates from the rectification voltage, the ratio of C_s/C_a allows us to obtain a $h_{DL}/(h_{FL}+h_{Oe})$ value of 19.4. The precise $h_{DL}/(h_{FL}+h_{Oe})$ value can be obtained as 6.8 through A_s/A_a for the IP mode case. This comparison reveals that, for the OOP mode, the $\sin\varphi$ term contains not only the rectification signal, which is only 35% of the total. The remaining 65% is from the spin-pumping contribution, which should also be considered.

The strong ISHE signal appearing in the OOP mode, rather than IP mode, can be explained and estimated by using Eq. (7); this signal exhibits an angular dependence of $\sin\varphi$ due to the dampinglike torque. First, we should obtain the tilted angle θ of the magnetization precession axis and the cone angle. From our previous work [29], we obtain the first- and second-order PMA fields as $H_1 = -1.67$ kOe and $H_2 = 12.6$ Oe. According to the principle of energy minimization, the tilted angle can be determined to be $\theta = 27°$ under the conditions of the resonance field $H_r = 1.48$ kOe. Under the condition of the FMR and rotational angle $\varphi = 90°$, the cone angles are deduced to be

$$\varphi_c = \frac{\omega/\gamma\,\Delta H}{H_{y'} + H_{z'}}(h_{FL} + h_{Oe})\sin\theta, \tag{10a}$$

$$\theta_c = \frac{\omega/\gamma\,\Delta H}{H_{y'} + H_{z'}}h_{DL}\sin\theta, \tag{10b}$$

Clearly, the OOP mode is mainly driven by stronger DL torque because h_{DL} is much larger than $h_{FL}+h_{Oe}$ in the $W/Co_{40}Fe_{40}B_{20}/MgO/Ta$ systems. Moreover, V_{ISHE} is almost equal to zero when the angle is $\theta = 0°$, while the cone angle of magnetization precession will have a sizeable value when the angle is $\theta = 27°$. This is why the OOP mode can give rise to a large value of V_{ISHE}, which is proportional to the square of the cone angle and maximized when the magnetization precession axis is oblique to the film plane.

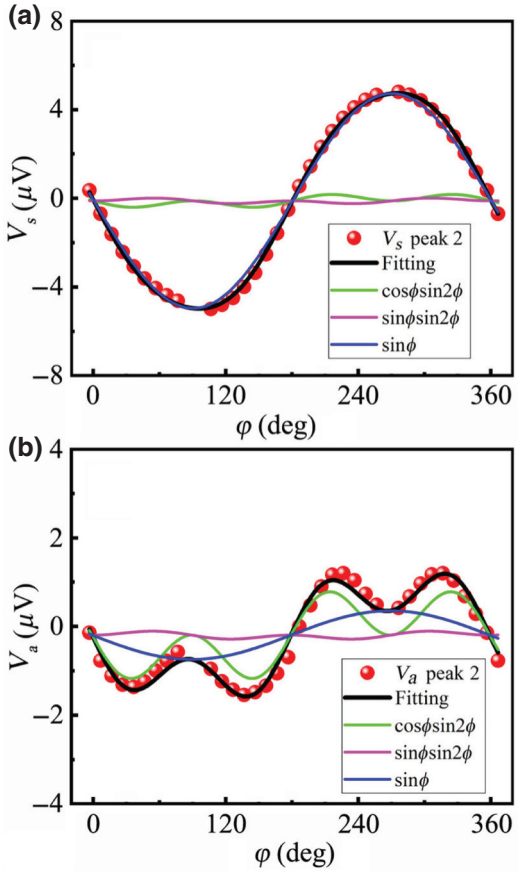

FIG. 4. Angular dependence of symmetric and antisymmetric components of the OOP mode. V_s (a) and V_a (b) distinctly contain angle relations of $\cos\varphi\sin2\varphi$ and $\sin\varphi$.

To estimate the spin Hall angle from V_{ISHE} (65% of the C_s), some parameters need to be determined. The rf Oersted field is calculated to be $h_{Oe} = t_{HM}J_c/2 = 0.89$ Oe when the amplitude of rf current density is $J_{rf} = 2.8 \times 10^{10}$ A/m^2, as estimated by measuring the power loss of the device. Therefore, the cone angle θ_c can be obtained as $\theta_c \approx 0.02$ rad. The effective spin-mixing conductance $G_{\uparrow\downarrow}$ is calculated to be $2.83 \times 10^{14}\,\Omega^{-1}\,m^{-2}$ by considering the resonance line width (see Appendix D for details) and the spin-diffusion length of tungsten is $\lambda_{sd} = 3.5$ nm with reference to the literature value [42]. Therefore, by using Eq. (7), the spin Hall angle can be estimated to be $\theta_{SH} = -0.68$. Notably, θ_{SH} obtained in the spin-pumping experiment is an intrinsic value [36]. We can further obtain the interfacial spin transparency T_{in} from [43]

$$T_{in} = 2G^{\uparrow\downarrow}\tanh\left(\frac{d}{2\lambda_{sd}}\right)\Big/\left[\frac{1}{\rho_{HM}\lambda_{sd}} + 2G^{\uparrow\downarrow}\coth\left(\frac{d}{\lambda_{sd}}\right)\right], \tag{11}$$

where $G_{\uparrow\downarrow}$ is the spin-mixing conductance, and d, λ_{sd}, and ρ_{HM} are the thickness, spin-diffusion length, and resistivity of the HM layer, respectively. The T_{in} values are 0.45 and 0.47 for the annealed samples and as-grown samples, respectively. Therefore, the ξ_{DL} value can be determined from $\xi_{DL} = T_{in}\cdot\theta_{SH} = -0.31$. The obtained ξ_{DL} value is consistent with that from the IMA system and MOD method. The successful extraction of the ISHE contribution in the OOP mode also indicates that ST FMR can be used to study the spin-pumping effect for the PMA sample. Overall, the obtained values from different methods for IMA and PMA samples are self-consistent. Our

results demonstrate the feasibility of obtaining SOT efficiency in the PMA sample through SMR-based ST FMR measurements.

V. CONCLUSIONS

We conduct a full analysis of SMR-based ST FMR for $W/Co_{40}Fe_{40}B_{20}/MgO$ samples with IMA and PMA. The SOT efficiencies for the IMA system are determined as reference values ($\xi_{DL} = -0.35$ and $\xi_{FL} = -0.05$) by analyzing the FM thickness dependence of SOT efficiency. Then, for the PMA sample, the ST FMR spectra present the IP and OOP modes. The DL torque efficiency is determined to be -0.38 by using the MOD method for the IP mode, which is consistent with the reference value. The OOP mode is also analyzed andt the dominant contribution comes from the spin-pumping-induced ISHE, and thus, a DL torque efficiency of -0.31 is obtained. In this experiment, the DL torque efficiency values obtained by different means are self-consistent. The successful determination of SOT efficiency in the PMA materials give insights to ST FMR studies of SOT efficiency.

ACKNOWLEDGMENTS

This work is supported by the National Key Research and Development Program of China (Grants No. 2017 YFA0206200 and No. 2018YFB0407600), the National Natural Science Foundation of China (NSFC, Grants No. 11874409, No. 11804380, No. 11434014, No. 51831012, and No. 51701203), the Beijing Natural Science Foundation (Grant No. Z190009), and partially supported by the Strategic Priority Research Program (B) (Grant No. XDB07030200), the Key Research Program of Frontier Sciences (Grant No. QYZDJ-SSW-SLH016), the International Partnership Program (Grant No. 112111KYSB20170090) of the Chinese Academy of Sciences (CAS), and Fujian Innovation Academy, Chinese Academy of Sciences (Grant No. FJCXY18040302).

APPENDIX A: ESTIMATION OF THE PRECESSION CONE ANGLE

The ferromagnetic resonance is driven by both the current-induced Oersted field and SOTs. The magnetization dynamic under these driving forces is governed by the Landau-Lifshitz-Gilbert (LLG) equation:

$$\frac{d\mathbf{m}}{dt} = -\gamma \mathbf{m}\times\mathbf{H}_{\text{eff}} + \alpha \mathbf{m} \times \frac{d\mathbf{m}}{dt} - \gamma \mathbf{m} \times \mathbf{h}_{\text{Oe}} + \tau_{\text{SOT}} \tag{A1}$$

where $\tau_{\text{SOT}} = \gamma(h_{\text{DL}}\mathbf{m} \times \sigma \times \mathbf{m} + h_{\text{FL}}\mathbf{m} \times \sigma)$ is the SOT, γ is the gyromagnetic ratio, α is the Gilbert damping coefficient, $\mathbf{H}_{\text{eff}}$ is the effective field, and $\mathbf{h}_{\text{Oe}}$ is the rf Oersted field. According to Ampere's law, under the condition that the sample width is much larger than the HM thickness t_{HM}, the Oersted field can be written as $\mathbf{h}_{\text{Oe}} = (t_{\text{HM}}J_c/2)\hat{\mathbf{y}}$. In the X', Y', Z' coordinate, the rf driving force can be transformed into

$$\mathbf{h}'_{\text{rf}} = \begin{bmatrix} (h_{\text{Oe}} + h_{\text{FL}})\cos\theta\sin\varphi \\ (h_{\text{Oe}} + h_{\text{FL}})\cos\varphi + h_{\text{DL}}\sin\theta\sin\varphi \\ h_{\text{DL}}\cos\varphi - (h_{\text{Oe}} + h_{\text{FL}})\sin\theta\sin\varphi \end{bmatrix}. \tag{A2}$$

Because the source of the rf Oersted field and rf SOT all originate from the rf charge current, only the magnitude and direction are different, so it is convenient to consider the response of $M_{y'}$ and $M_{z'}$ to rf driving force as the same susceptibility χ in the X', Y', Z' coordinate. The susceptibility $\chi(H)$ can be obtained by solving the LLG equation in the linear response regime [44]

$$\chi = (L + iD)C_0 \begin{pmatrix} 0 & 0 & 0 \\ 0 & 1 - iC_1 & C_2 \\ 0 & -C_2 & 1 - iC_3 \end{pmatrix}, \tag{A3}$$

where the L and D functions are

$$L = \frac{\Delta H^2}{(H - H_r)^2 + \Delta H^2}, \tag{A4}$$

$$D = \frac{\Delta H(H - H_r)}{(H - H_r)^2 + \Delta H^2}, \tag{A5}$$

where H_r is the resonance field and $\Delta H = \alpha\omega/\gamma$ is the line width; the real numbers C_0–C_3 are $C_0 = M_0/(H_{y'} + H_{z'})$, $C_1 = H_{z'}/\Delta H$, $C_2 = 1/\alpha$, and $C_3 = H_{y'}/\Delta H$. Here, $H_{y'}$ and $H_{z'}$ are the static effective fields formed by the external field and magnetic anisotropy field, respectively, in the X', Y', Z' coordinate. Hence, the cone angle $\varphi_c \approx M_{y'}/M_0$ and $\theta_c \approx M_{z'}/M_0$ can be deduced [45,46]

$$\begin{aligned} &\alpha(H_{y'} + H_{z'})\varphi_c \\ &\quad = [h_{\text{DL}}\cos\varphi - (h_{\text{Oe}} + h_{\text{FL}})\sin\theta\sin\varphi]L \\ &\qquad + \sqrt{\frac{H_{z'}}{H_{y'}}}[(h_{\text{Oe}} + h_{\text{FL}})\cos\varphi + h_{\text{DL}}\sin\theta\sin\varphi]D, \end{aligned} \tag{A6}$$

$$\begin{aligned} &\alpha(H_{y'} + H_{z'})\theta_c \\ &\quad = [-h_{\text{DL}}\sin\theta\sin\varphi - (h_{\text{Oe}} + h_{\text{FL}})\cos\varphi]L \\ &\qquad + \sqrt{\frac{H_{y'}}{H_{z'}}}[h_{\text{DL}}\cos\varphi - (h_{\text{Oe}} + h_{\text{FL}})\sin\theta\sin\varphi]D. \end{aligned} \tag{A7}$$

APPENDIX B: EXTERNAL FIELD H DEPENDENCE OF ΔR_{SMR}

Figure 5 shows $\Delta R_{\text{SMR}}/R_{\text{max}}$ at different external fields for the ultrathin FM layer with PMA, which is extracted

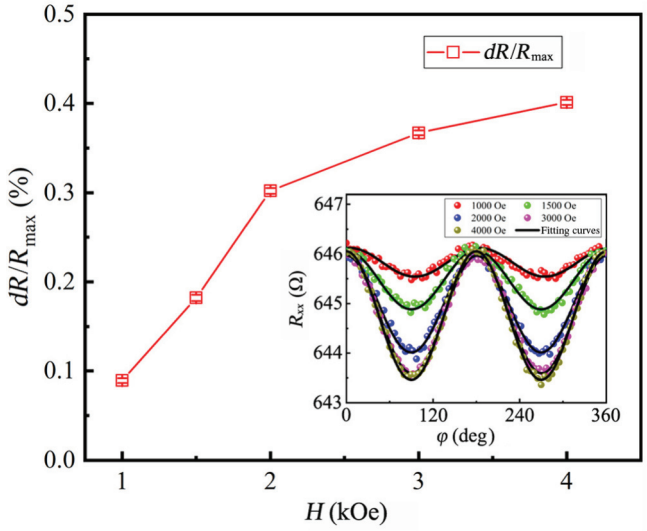

FIG. 5. SMR at different external fields for the ultrathin film with PMA. Inset is the angular dependence of device resistance at different external fields.

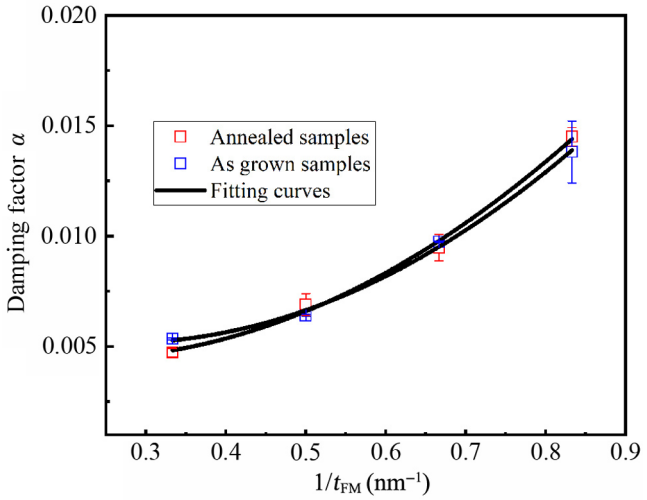

FIG. 6. Damping coefficient as a function of t_{FM}^{-1} for annealed and as-grown samples. Black solid lines are fitting curves obtained by using Eq. (D1).

from the device resistance during rotation of the external field in the film plane, as shown in the inset of Fig. 5. It is obvious that $\Delta R/R_{\mathrm{max}}$ increases gradually with an increase in the external field due to the reduction of angle θ between magnetization **M** and the film plane. The $\Delta R_{\mathrm{SMR}}/R_{\mathrm{max}}$ value at resonance field $H_r = 3000$ Oe is 0.37%; this value is twice as large as that of $\Delta R_{\mathrm{SMR}}/R_{\mathrm{max}} = 0.18\%$ at resonance field $H_r = 1500$ Oe.

APPENDIX C: PARASITIC VOLTAGE FROM INVERSE SPIN HALL EFFECT

In ST FMR measurements, the ISHE due to spin pumping also contributes to the measured voltage. The spin-pumping-induced parasitic voltages also have the same angular dependence $\cos\varphi\sin 2\varphi$ as that of the symmetric component of ST FMR voltage. Therefore, we need to consider the proportion of V_{ISHE} in the ST FMR voltage $V_{\mathrm{ST\,FMR}}^{\mathrm{sym}}$. According to the theory of ISHE and ST FMR, the ratio of $V_{\mathrm{ISHE}}/V_{\mathrm{ST\,FMR}}^{\mathrm{sym}}$ can be estimated by [47,48]

$$\frac{V_{\mathrm{ISHE}}}{V_{\mathrm{ST\,FMR}}^{\mathrm{sym}}} = \frac{2L\lambda_N e^2 \mu_0 M_0 \omega g_{\mathrm{eff}}^{\uparrow\downarrow} (df/dH)_{H=H_r} t_F t_N^2 \sigma_N}{(dR/d\varphi)\gamma W \hbar \Delta H (t_N\sigma_N + t_F\sigma_F)^2} \times \tanh\left(\frac{t_N}{2\lambda_N}\right), \tag{C1}$$

where $g_{\mathrm{eff}}^{\uparrow\downarrow}$ and λ_N are the effective spin-mixing conductance and spin-diffusion length, respectively. t_N, t_F, σ_N, and σ_F are the thickness of the heavy-metal layer, the thickness of the ferromagnetic layer, the conductivity of the heavy-metal layer, and the conductivity of the ferromagnetic layer. L and W are the length and width of the sample, respectively. Here, we define the proportion of ISHE voltage in the total voltage as $\eta \equiv V_{\mathrm{ISHE}}/(V_{\mathrm{ISHE}} + V_{\mathrm{ST\,FMR}}^{\mathrm{sym}})$. From Eq. (C1), we can calculate the proportion of the contribution from ISHE to be less than 5% for our samples. Therefore, for the analysis of the angular dependence of $\cos\varphi\sin 2\varphi$, we ignore the contribution from the ISHE due to spin pumping in the present work.

APPENDIX D: ESTIMATION OF SPIN-MIXING CONDUCTANCE $G^{\uparrow\downarrow}$

The effective spin-mixing conductance is closely related to the enhancement of the damping constant due to interfacial spin-orbit coupling, which can be expressed as [49]

$$\alpha = \alpha_0 + G_{\mathrm{eff}}^{\uparrow\downarrow} \frac{g\mu_B h}{4\pi M_0 e^2} t_{\mathrm{FM}}^{-1} + \beta_{\mathrm{TMS}} t_{\mathrm{FM}}^{-2}, \tag{D1}$$

where α_0 represents the intrinsic damping constant, g is the g factor, μ_B is the Bohr magnetron, and h is Planck's constant; β_{TMS} is a coefficient that depends on the two-magnon scattering. By fitting the t_{FM}^{-1} dependence of damping α, as shown in Fig. 6, we obtain intrinsic damping $\alpha_0 = 0.005$ and effective $G^{\uparrow\downarrow} = 2.83 \times 10^{14}\,\Omega^{-1}\,\mathrm{m}^{-2}$ for the annealed samples, as well as $\alpha_0 = 0.007$ and effective $G^{\uparrow\downarrow} = 3.81 \times 10^{14}\,\Omega^{-1}\,\mathrm{m}^{-2}$ for the as-grown samples.

[1] I. M. Miron, K. Garello, G. Gaudin, P.-J. Zermatten, M. V. Costache, S. Auffret, S. Bandiera, B. Rodmacq, A. Schuhl, and P. Gambardella, Perpendicular switching of a single ferromagnetic layer induced by in-plane current injection, Nature **476**, 189 (2011).

[2] L. Q. Liu, Chi-Feng Pai, Y. Li, H. W. Tseng, D. C. Ralph, and R. A. Buhrman, Spin-torque switching with the giant spin hall effect of tantalum, Science **336**, 555 (2012).

[3] G. Yu, P. Upadhyaya, Y. Fan, J. G. Alzate, W. Jiang, K. L. Wong, S. Takei, S. A. Bender, L.-T. Chang, Y. Jiang, M. Lang, J. Tang, Y. Wang, Y. Tserkovnyak, P. K. Amiri, and K. L. Wang, Switching of perpendicular magnetization by spin–orbit torques in the absence of external magnetic fields, Nat. Nanotechnol. **9**, 548 (2014).

[4] A. A. Awad, P. Dürrenfeld, A. Houshang, M. Dvornik, E. Iacocca, R. K. Dumas, and J. Åkerman, Long-range mutual synchronization of spin hall nano-oscillators, Nat. Phys. **13**, 292 (2017).

[5] S. Bhuktare, H. Singh, A. Bose, and A. A. Tulapurkar, Spintronic Oscillator Based on Spin-Current Feedback Using the Spin Hall Effect, Phys. Rev. Appl. **7**, 014022 (2017).

[6] C. Safranski, E. A. Montoya, and I. N. Krivorotov, Spin-orbit torque driven by a planar hall current, Nat. Nanotechnol. **14**, 27 (2019).

[7] T. Shiino, S.-H. Oh, P. M. Haney, S.-W. Lee, G. Go, B.-G. Park, and K.-J. Lee, Antiferromagnetic Domain Wall Motion Driven by Spin-Orbit Torques, Phys. Rev. Lett. **117**, 087203 (2016).

[8] G. Yu, P. Upadhyaya, X. Li, W. Li, S. K. Kim, Y. Fan, K. L. Wong, Y. Tserkovnyak, P. K. Amiri, and K. L. Wang, Room-Temperature creation and spin-orbit torque manipulation of skyrmions in thin films with engineered asymmetry, Nano Lett. **16**, 1981 (2016).

[9] G. Yu, P. Upadhyaya, Q. Shao, H. Wu, G. Yin, X. Li, C. He, W. Jiang, X. Han, P. K. Amiri, and K. Wang, Room-Temperature skyrmion shift device for memory application, Nano Lett. **17**, 261 (2017).

[10] C.-F. Pai, Y. Ou, L. H. Vilela-Leão, D. C. Ralph, and R. A. Buhrman, Dependence of the efficiency of spin hall torque on the transparency of Pt/ferromagnetic layer interfaces, Phys. Rev. B **92**, 064426 (2015).

[11] Y. Ou, C.-F. Pai, S. Shi, D. C. Ralph, and R. A. Buhrman, Origin of fieldlike spin-orbit torques in heavy metal/ferromagnet/oxide thin film heterostructures, Phys. Rev. B **94**, 140414(R) (2016).

[12] T. Gao, A. Qaiumzadeh, H. An, A. Musha, Y. Kageyama, J. Shi, and K. Ando, Intrinsic Spin-Orbit Torque Arising From the Berry Curvature in a Metallic-Magnet/Cu-Oxide Interface, Phys. Rev. Lett. **121**, 017202 (2018).

[13] K. Garello1, I. M. Miron, C. O. Avci1, F. Freimuth, Y. Mokrousov, S. Blügel, S. Auffret, O. Boulle, G. Gaudin, and P. Gambardella, Symmetry and magnitude of spin–orbit torques in ferromagnetic heterostructures, Nat. Nanotechnol. **8**, 587 (2013).

[14] S. Fukami, T. Anekawa, C. Zhang, and H. Ohno, A spin–orbit torque switching scheme with collinear magnetic easy axis and current configuration, Nat. Nanotechnol. **11**, 621 (2016).

[15] M. Cubukcu, O. Boulle, M. Drouard, K. Garello, C. O. Avci, I. M. Miron, J. Langer, B. Ocker, P. Gambardella, and G. Gaudin, Spin-orbit torque magnetization switching of a three-terminal perpendicular magnetic tunnel junction, Appl. Phys. Lett. **104**, 042406 (2014).

[16] K. Garello, C. O. Avci, I. M. Miron, M. Baumgartner, A. Ghosh, S. Auffret, O. Boulle, G. Gaudin, and P. Gambardella, Ultrafast magnetization switching by spin-orbit torques, Appl. Phys. Lett. **105**, 212402 (2014).

[17] U. H. Pi, K. W. Kim, J. Y. Bae, S. C. Lee, Y. J. Cho, K. S. Kim, and S. Seo, Tilting of the spin orientation induced by rashba effect in ferromagnetic metal layer, Appl. Phys. Lett. **97**, 162507 (2010).

[18] M. Hayashi, J. Kim, and M. Y. H. Ohno, Quantitative characterization of the spin-orbit torque using harmonic hall voltage measurements, Phys. Rev. B **89**, 144425 (2014).

[19] J. C. Sankey, Y.-T. Cui, J. Z. Sun, J. C. Slonczewski, R. A. Buhrman, and D. C. Ralph, Measurement of the spin-transfer-torque vector in magnetic tunnel junctions, Nat. Phys. **4**, 67 (2008).

[20] H. Kubota, A. Fukushima, K. Yakushiji, T. Nagahama, S. Yuasa, K. Ando, H. Maehara, Y. Nagamine, K. Tsunekawa, D. D. Djayaprawira, N. Watanabe, and Y. Suzuki, Quantitative measurement of voltage dependence of spin-transfer torque in MgO-based magnetic tunnel junctions, Nat. Phys. **4**, 37 (2008).

[21] L. Q. Liu, T. Moriyama, D. C. Ralph, and R. A. Buhrman, Spin-Torque Ferromagnetic Resonance Induced by the Spin Hall Effect, Phys. Rev. Lett. **106**, 036601 (2011).

[22] X. Fan, H. Celik, J. Wu, C. Ni, K. J. Lee, V. O. Lorenz, and J. Q. Xiao, Quantifying interface and bulk contributions to spin-orbit torque in magnetic bilayers, Nat. Commun. **5**, 3042 (2014).

[23] Y. Li, H. Saglam, Z. Zhang, R. Bidthanapally, Y. Xiong, John E. Pearson, V. Novosad, H. Qu, G. Srinivasan, A. Hoffmann, and W. Zhang, Simultaneous Optical and Electrical Spin-Torque Magnetometry with Phase-Sensitive Detection of Spin Precession, Phys. Rev. Appl. **11**, 034047 (2019).

[24] C.-F. Pai, L. Liu, Y. Li, H. W. Tseng, D. C. Ralph, and R. A. Buhrman, Spin transfer torque devices utilizing the giant spin hall effect of tungsten, Appl. Phys. Lett. **101**, 122404 (2012).

[25] C.-F. Pai, M.-H. Nguyen, C. Belvin, L. H. Vilela-Leão, D. C. Ralph, and R. A. Buhrman, Enhancement of perpendicular magnetic anisotropy and transmission of spin-hall-effect-induced spin currents by a Hf spacer layer in W/Hf/CoFeB/MgO layer structures, Appl. Phys. Lett. **104**, 082407 (2014).

[26] J. Kim, D. Lee, K.-J. Lee, B.-K. Ju, H. C. Koo, B.-C. Min, and O. Lee, Spin-orbit torques associated with ferrimagnetic order in Pt/GdFeCo/MgO layers, Sci. Rep. **8**, 6017 (2018).

[27] H. Nakayama, M. Althammer, Y.-T. Chen, K. Uchida, Y. Kajiwara, D. Kikuchi, T. Ohtani, S. Geprägs, M. Opel, S. Takahashi, R. Gross, G. E. W. Bauer, S. T. B. Goennenwein, and E. Saitoh, Spin Hall Magnetoresistance Induced by a Nonequilibrium Proximity Effect, Phys. Rev. Lett. **110**, 206601 (2013).

[28] M. Schreier, T. Chiba, A. Niedermayr, J. Lotze, H. Huebl, S. Geprägs, S. Takahashi, G. E. W. Bauer, R. Gross, and S. T. B. Goennenwein, Current-induced spin torque resonance of a magnetic insulator, Phys. Rev. B **92**, 144411 (2015).

[29] C. He, A. Navabi, Q. Shao, G. Yu, D. Wu, W. Zhu, C. Zheng, X. Li, Q. L. He, S. A. Razavi, K. L. Wong, Z. Zhang, P. K. Amiri, and K. L. Wang, Spin-torque

ferromagnetic resonance measurements utilizing spin hall magnetoresistance in $W/Co_{40}Fe_{40}B_{20}/MgO$ structures, Appl. Phys. Lett. **109**, 202404 (2016).

[30] C. He, G. Yu, C. Grezes, J. Feng, Z. Zhao, S. A. Razavi, Q. Shao, A. Navabi, X. Li, Q. L. He, M. Li, J. Zhang, K. L. Wong, D. Wei, G. Zhang, X. Han, P. K. Amiri, and K. L. Wang, Spin-Torque Ferromagnetic Resonance in W/Co-Fe-B/W/Co-Fe-B/MgO Stacks, Phys. Rev. Appl. **10**, 034067 (2018).

[31] J. Sklenar, W. Zhang, M. B. Jungfleisch, W. J. Jiang, H. C. Chang, J. E. Pearson, M. Z. Wu, J. B. Ketterson, and A. Hoffmann, Driving and detecting ferromagnetic resonance in insulators with the spin hall effect, Phys. Rev. B **92**, 174406 (2015).

[32] C. O. Avci, K. Garello, A. Ghosh, M. Gabureac, S. F. Alvarado, and P. Gambardella, Unidirectional spin hall magnetoresistance in ferromagnet/normal metal bilayers, Nat. Phys. **11**, 570 (2015).

[33] J. Fischer, O. Gomonay, R. Schlitz, K. Ganzhorn, N. Vlietstra, M. Althammer, H. Huebl, M. Opel, R. Gross, S. T. B. Goennenwein, et al., Spin hall magnetoresistance in antiferromagnet/heavy-metal heterostructures, Phys. Rev. B **97**, 014417 (2018).

[34] I. Barsukov, Y. Fu, A. M. Gonçalves, M. Spasova, M. Farle, L. C. Sampaio, R. E. Arias, and I. N. Krivorotov, Field-dependent perpendicular magnetic anisotropy in CoFeB thin films, Appl. Phys. Lett. **105**, 152403 (2014).

[35] H. Zhou, X. Fan, L. Ma, Q. Zhang, L. Cui, S. Zhou, Y. S. Gui, C.-M. Hu, and D. Xue, Spatial symmetry of spin pumping and inverse spin hall effect in the $Pt/Y_3Fe_5O_{12}$ system, Phys. Rev. B **94**, 134421 (2016).

[36] O. Mosendz, J. E. Pearson, F. Y. Fradin, G. E. Bauer, S. D. Bader, and A. Hoffmann, Quantifying Spin Hall Angles From Spin Pumping: Experiments and Theory, Phys. Rev. Lett. **104**, 046601 (2010).

[37] Q. Hao and G. Xiao, Giant Spin Hall Effect and Switching Induced by Spin-Transfer Torque in a $W/Co_{40}Fe_{40}B_{20}/MgO$ Structure with Perpendicular Magnetic Anisotropy, Phys. Rev. Appl. **3**, 034009 (2015).

[38] W. Skowroński, M. Cecot, J. Kanak, S. Zietek, T. Stobiecki, L. Yao, S. van Dijken, T. Nozaki, K. Yakushiji, and S. Yuasa, Temperature dependence of spin-orbit torques in W/CoFeB bilayers, Appl. Phys. Lett. **109**, 062407 (2016).

[39] J. Sklenar, W. Zhang, M. B. Jungfleisch, H. Saglam, S. Grudichak, W. Jiang, J. E. Pearson, J. B. Ketterson, and A. Hoffmann, Unidirectional spin-torque driven magnetization dynamics, Phys. Rev. B **95**, 224431 (2017).

[40] K. Ando, S. Takahashi, J. Ieda, Y. Kajiwara, H. Nakayama, T. Yoshino, K. Harii, Y. Fujikawa, M. Matsuo, S. Maekawa, and E. Saitoh, Inverse spin-hall effect induced by spin pumping in metallic system, J. Appl. Phys. **109**, 103913 (2011).

[41] S. Emori, A. Matyushov, H.-M. Jeon, C. J. Babroski, T. Nan, A. M. Belkessam, John G. Jones, M. E. McConney, G. J. Brown, B. M. Howe, and N. X. Sun, Spin-orbit torque and spin pumping in YIG/Pt with interfacial insertion layers, Appl. Phys. Lett. **112**, 182406 (2018).

[42] Q. Hao, W. Chen, and G. Xiao, Beta (β) tungsten thin films: Structure, electron transport, and giant spin hall effect, Appl. Phys. Lett. **106**, 182403 (2015).

[43] Q. Shao, C. Tang, G. Yu, A. Navabi, H. Wu, C. He, J. Li, P. Upadhyaya, P. Zhang, S. A. Razavi, et al., Role of dimensional crossover on spin-orbit torque efficiency in magnetic insulator thin films, Nat. Commun. **9**, 3612 (2018).

[44] Y. Zhang, Q. Liu, B. F. Miao, H. F. Ding, and X. R. Wang, Anatomy of electrical signals and dc-voltage line shape in spin-torque ferromagnetic resonance, Phys. Rev. B **99**, 064424 (2019).

[45] Y. Guan, W. E. Bailey, E. Vescovo, C. C. Kao, and D. A. Arena, Phase and amplitude of element-specific moment precession in $Ni_{81}Fe_{19}$, J. Magn. Magn. Mater. **312**, 374 (2007).

[46] J. Sklenar1, W. Zhang, M. B. Jungfleisch, A. Hoffmann, Unidirectional response in spin-torque driven magnetization dynamics, Proc. SPIE 10732, Spintronics XI, 1073212 (2018).

[47] K. Kondou, H. Sukegawa, S. Kasai, S. Mitani, Y. Niimi, and Y. Otani, Influence of inverse spin hall effect in spin-torque ferromagnetic resonance measurements, Appl. Phys. Express **9**, 023002 (2016).

[48] A. Kumar, S. Akansel, H. Stopfel, M. Fazlali, J. Åkerman, R. Brucas, and P. Svedlindh, Spin transfer torque ferromagnetic resonance induced spin pumping in the Fe/Pd bilayer system, Phys. Rev. B **95**, 064406 (2017).

[49] L. Zhu, D. C. Ralph, and R. A. Buhrman, Effective Spin-Mixing Conductance of Heavy-Metal-Ferromagnet Interfaces, Phys. Rev. Lett. **123**, 057203 (2019).